Journal of Physics D: Applied Physics

PAPER

Gyromagnetic ratio of oriented hcp $Co_{1-x}Ir_x$ soft magnetic films

To cite this article: Sha Zhang *et al* 2021 *J. Phys. D: Appl. Phys.* **54** 505005

IOP Publishing Journal of Physics D: Applied Physics

J. Phys. D: Appl. Phys. **54** (2021) 505005 (9pp) https://doi.org/10.1088/1361-6463/ac1ddd

Gyromagnetic ratio of oriented hcp $Co_{1-x}Ir_x$ soft magnetic films

Sha Zhang[1,2], Ting Fu[1], Tao Wang[1], Xiaolong Fan[1], Meizhen Gao[1,*], Zhiwei Li[1,*] and Fashen Li[1]

[1] Institute of Applied Magnetics, Key Laboratory of Magnetism and Magnetic Materials of Ministry of Education, Lanzhou University, Lanzhou 730000, People's Republic of China
[2] The Key Laboratory of Physics and Photoelectric Information Functional Materials, North Minzu University, Yinchuan 750021, People's Republic of China

E-mail: gaomz@lzu.edu.cn and zweili@lzu.edu.cn

Received 15 June 2021, revised 12 August 2021
Accepted for publication 16 August 2021
Published 29 September 2021

Abstract

The gyromagnetic ratio γ is a key quantity that determines spin and magnetic properties. In this study, γ is investigated via the electric detection of ferromagnetic resonance and first-principles calculations for *c*-axis oriented hcp-$Co_{1-x}Ir_x$ ($0.00 \leqslant x \leqslant 0.23$) soft magnetic films with easy-plane magnetocrystalline anisotropy. γ increases linearly from 19.13 GHz kOe^{-1} for pure Co film to 19.32 GHz kOe^{-1} at $x = 0.23$, which is in agreement with the calculated result. The calculations reveal that the primary reason for the variation of γ is the different trends in the spin and orbital magnetic moments of the neighboring Co atoms of Ir, especially the linear increase of the latter. An investigation into the electronic structure indicates that the increase in these orbital magnetic moments is due to the appearance of 3*d* unoccupied minority states moving towards the Fermi level, which is induced by the local lattice distortion centered at Ir. Our findings provide the important γ data for the applications of CoIr soft magnetic films in high-frequency electromagnetic and spintronic devices, and will provide guidance in the understanding of the dynamic magnetic properties in disordered binary magnetic alloys.

Keywords: gyromagnetic ratio, Hcp $Co_{1-x}Ir_x$ alloys, ferromagnetic resonance, soft magnetic films, first-principles calculation

(Some figures may appear in colour only in the online journal)

1. Introduction

Soft magnetic films have attracted significant attention owing to their potential application to various high-frequency electromagnetic and spintronic devices, such as microwave absorbers, micro-transformers, recording media, magnetic memories, and spin valve devices [1–5]. Of the spin and magnetic properties that determine these practical applications, the gyromagnetic ratio (γ) is an important quantity, which corresponds to the Landé g factor ($\gamma = g\frac{e\mu_0}{2m_e}$, where m_e is electron mass and μ_0 is the permeability of vacuum) [6, 7]. γ is one of the fundamental quantities that characterize the high-frequency response of a ferromagnetic material, particularly for determining the natural resonance frequency (f_r) [8, 9]. γ (g factor) is necessary for the manipulation of spin dynamics and resonance [10–13], and it is an important tool for electronic structure investigation because it is directly related to the ratio of the orbital and spin momentums, as well as the spin-splitting energy [7, 8, 11, 14].

Owing to the importance of γ and the increasing interest in spintronics and new schemes for quantum computation [15], γ has recently been the subject of many experimental and theoretical studies [11, 13, 16–19]. In the experimental studies, quantum beating spectroscopy, Kerr rotation, and electrically detected electron spin resonance (ESR) techniques were primarily used for the investigation of γ; the electrically detected ESR technique is particularly suitable for

* Authors to whom any correspondence should be addressed.

precise measurements in magnetic films [7, 14]. Moreover, the utilization of electric detection of ferromagnetic resonance (FMR) has recently demonstrated reliability and validity in the study of γ (measured using a direct current (dc) electrical method) in magnetic films [12, 13, 18–20]. Because γ corresponds to the g factor, theoretical studies primarily investigate the g factor instead of γ [6, 16]. For materials with considerably strong spin-orbital coupling, such as magnetic materials, g factor can be studied via their significant spin and orbital magnetic moments [21]. For materials that have an energy band gap, such as semiconductors, g factor is discussed with the aid of the spin-splitting energy between the highest occupied and lowest unoccupied states [6, 10, 11].

Among the known soft magnetic films, close-packed hexagonal (*hcp*) CoIr films with grains that have a *c*-axis perpendicular to the film plane are a type of soft magnetic material with high easy-plane magnetocrystalline anisotropy energy that have been attracting special research interest. They are proven to be effective in increasing f_r without decreasing the high initial permeability (μ_i) [22], in maintaining magnetic moments strictly lying in the film plane, as well as the Néel wall for thick films [5], and in achieving improved effects in recording medias [1, 23–25]. As an importance parameter, γ is involved in most of the reported works of CoIr films. However, few works consider the accurate value of γ, but roughly set it as 17.6 GHz kOe^{-1} ($g = 2$) [5, 9, 22, 23, 26–28]. To supplement the important γ data for CoIr soft magnetic films, in this study, the γ of oriented *hcp* $Co_{1-x}Ir_x$ ($0.00 \leqslant x \leqslant 0.23$) soft magnetic films is investigated according to the electric detection of FMR. Moreover, to understand the physical origin of the variation in γ, the magnetic moments, γ, and the electronic properties of these $Co_{1-x}Ir_x$ alloys are studied using first-principles calculation.

2. Methods

2.1. Experiment

All samples were prepared using the magnetron sputtering method with Si surface oxidation wafers as the substrate. The base pressure of the vacuum was smaller than 5.0×10^{-5} Pa. To improve the *c*-axis orientation of CoIr films, the samples were fabricated with a layered structure: substrate/Ta (8 nm)/Au (25 nm)/$Co_{1-x}Ir_x$ (35 nm)/Au (2 nm), where x changes from 0.00 to 0.23. The seed layers were deposited with an Ar pressure of 0.15 Pa. The $Co_{1-x}Ir_x$ layers were grown with an Ar pressure of 0.25 Pa by using the Co target with Ir pieces symmetrically placed on the erosion race-track, where the concentration of Ir can be manipulated by changing the number of Ir pieces. To induce an in-plane uniaxial anisotropy, the substrate was inclined using a 15° wedge during the sputtering process.

A surface profile meter (Dektak 8, Bruker, Billerica, MA, USA) and x-ray photoelectron spectroscopy were exploited to determine the film thicknesses d and composition of the samples, respectively. The x-ray diffraction technique (XRD, X'Pert PRO with Cu K_α radiation, Philips, Amsterdam, the Netherlands) was used to characterize the crystalline structure. The static magnetic properties were measured using the vibrating sample magnetometer. The films were magnetized along the in-plane easy axis before their complex permeability measurements (with a static magnetic field ~2.0 kOe from an permanent magnet), then the measurements were obtained using a vector network analyzer (E8363B, Agilent, Santa Clara, CA, USA) via the shorted micro-strip method. The gyromagnetic ratio of the films was obtained by fitting the FMR peaks, which were measured using an independently-built frequency-conversion FMR system [13]. For this measurement, a microwave generator (SMF 100 A, Rohde & Schwarz, Munich, Germany) was used to inject a radio frequency (RF) current (4–20 GHz) into the CoIr strip samples, which were magnetized along the in-plane direction (with a quasistatic magnetic field with a maximum value of ~2 T from an electromagnet). The rectified voltage, recorded as the derivative of the microwave power absorption with respect to the applied field, was measured using the lock-in amplifier (SR830, Stanford Research Systems, Sunnyvale, CA, USA) [18]. To increase the signal-to-noise ratio, quasistatic dc magnetic field was modulated using the ac magnetic field of 0.05 kOe with a low frequency of 875 Hz.

2.2. Calculation method

We performed the first-principles density functional theory calculations using the full potential linearized augmented plane wave method, as embodied in the WIEN2K code [29]. The generalized gradient approximation with the Perdew–Burke–Wang form was employed for the exchange-correlation effects [30]. The band states and core-level states are treated with scalar relativistic effects and fully relativistic effects, respectively. The muffin-tin radii (R_{mt}) were 2.20 and 2.32 a.u. for Co and Ir atoms, respectively. The wave functions were described by spherical harmonics inside the muffin-tin spheres, and plane waves in the interstitial region. The maximum angular momenta (l_{max}) for the expansion of the spherical harmonics was confined to $l_{max} = 10$. The cutoff parameter $R_{MT}K_{MAX}$ to limit the number of plane waves was set to 7.0. The magnitude of the largest vector in the Fourier expansion of the electron density (G_{max}) was 14.0.

Pure Co has an *hcp* lattice structure (the lattice constants are $a = 2.458$ Å and $c = 4.033$ Å) with the *c*-axis parallel to the *z*-axis of the Cartesian coordinate system. Based on this unit cell, the supercells of $Co_{0.97}Ir_{0.03}$, $Co_{0.94}Ir_{0.06}$, $Co_{0.87}Ir_{0.13}$, $Co_{0.83}Ir_{0.17}$, $Co_{0.81}Ir_{0.19}$, and $Co_{0.75}Ir_{0.25}$ were identified. As the main phase of the $Co_{1-x}Ir_x$ films experimentally exhibits a *c*-axis-oriented *hcp* structure, the *hcp* structure among all possible crystal structures was selected for all doping levels except $Co_{0.94}Ir_{0.06}$ (for $Co_{0.94}Ir_{0.06}$, the *hcp* structure is unreachable; therefore, the 63CmCm structure exhibiting the highest symmetry and lowest energy was chosen) [1]. Then, the volume and lattice parameters of the selected structures were optimized, and the atomic positions in each supercell were fully relaxed until the force on each atom was less than 5.0 mRy a^{-1} u. Subsequent to the test calculations of the energy convergence with respect to the number of *k*-points, the *k*-points were set to 800, 800, 6000, 8000, 1500, and 6000 for

$Co_{0.97}Ir_{0.03}$, $Co_{0.94}Ir_{0.06}$, $Co_{0.87}Ir_{0.13}$, $Co_{0.83}Ir_{0.17}$, $Co_{0.81}Ir_{0.19}$, and $Co_{0.75}Ir_{0.25}$, respectively. SCF calculations with spin-orbit (SO) coupling parallel to the (110)-axis (x-axis) were performed to obtain the γ of the ab-plane.

3. Results and discussion

3.1. The trend of γ

The composition dependence of the CoIr film XRD pattern is shown in figure 1. Only two peaks can be clearly observed: (111) peak of Au and the (002) peak of the $Co_{1-x}Ir_x$ layer. The unique (002) peak reveals that the oriented *hcp*-CoIr films with their c-axes perpendicular to the film plane are successfully realized. A significant left-drift of the (002) peak of $Co_{1-x}Ir_x$ is also observed with increasing Ir percent. The diffraction angle 2θ reduces from 44.47° to 43.73° as x increases from 0.00 to 0.23. According to the angle, the lattice constant c was obtained using the Bragg equation $c = n\lambda/(2\sin\theta)$[27], and the results are displayed with red round dots in the inset of figure 1. It can be observed that the constant c increases linearly with x, which indicates that Ir was successfully doped in *hcp* Co, as the atomic diameter of Ir is bigger than that of Co.

To obtain the static magnetic parameters of the $Co_{1-x}Ir_x$ films, the in-plane hysteresis loops were measured with an applied magnetic field parallel and perpendicular to the easy axis. The initial magnetization curves parallel and perpendicular to the film plane were also measured. As an example, figures 2(a) and (b) show the in-plane hysteresis loops and the initial magnetization curves of the $Co_{0.94}$ $Ir_{0.06}$ film, respectively. The films clearly exhibit good soft magnetic properties and in-plane uniaxial anisotropy. The saturation magnetizations (M_s) of the samples obtained from the hysteresis loops are denoted with red round dots in figure 2(c). M_s follows a linear variation with increasing x, and it reduces from 1470 Gs to 1002 Gs, which is in good agreement with the reported M_s [2, 28, 31]. The total out-of-plane anisotropy field (H_{out}) was obtained by calculating the area between two magnetization curves, as shown in figure 2(b). The results are displayed with red round dots in figure 2(d), and they are in accordance with those reported in our previous study within the error range [27]. H_{out} contains the demagnetization field ($4\pi M_s$) and the equivalent magnetocrystalline anisotropy field. Hence, the magnetocrystalline anisotropy constant (K_g) can be obtained through $K_g = -M_s(H_{out} - 4\pi M_s)/2$. A negative K_g means the CoIr film has easy-plane magnetocrystalline anisotropy, while a positive K_g indicates that the magnetization easy axis is along the c-axis. As x increases, K_g changes from positive to negative near $x = 0.06$, which is in agreement with previous literatures [23, 27, 28, 31]. The possible errors of K_g (as well as H_{out}) come from the so-called perpendicular anisotropy field [4], the surface roughness, the crystal orientation degree, and so on. Similar to H_{out}, the in-plane uniaxial anisotropy field (H_u) was also estimated, and it is denoted by blue diamonds in figure 2(d). Considering its small value, its accuracy will be influenced by the selected area of the samples, the accuracy in searching the easy (difficult) axis, the measurement conditions and instrument status, and so on. Therefore, the value of H_u in figure 2(d) is only for reference in the following discussion.

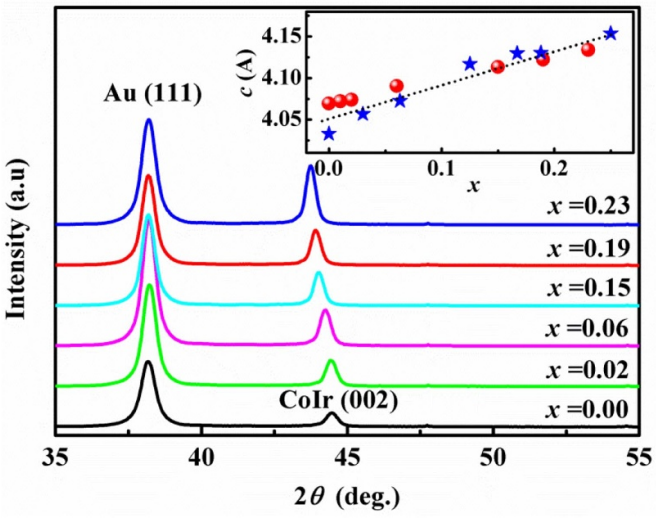

Figure 1. XRD pattern of the $Co_{1-x}Ir_x$ films. The inset displays the lattice constant c of the $Co_{1-x}Ir_x$ system obtained using XRD results (red round dots) and first-principles calculations (blue five-pointed stars), while the dotted line is for guidance.

In this study, we experimentally obtained the value of the gyromagnetic ratio by the dc electric detection of FMR. As shown in the inset of figure 3, the CoIr films were cut into 6 mm × 10 mm strips and fixed at the center of the detector. When an RF signal (5–20 GHz) was applied to the CoIr strip, an RF magnetic field was observed, which can push the spin into precession [32]. As a consequence of the rectification effect of the rectifier diode, a rectified dc voltage ($V' \propto dI_{FMR}/dH$) was detected in the strip, hence allowing the measurement of the resonance peaks associated with the spin dynamics [13].

Taking the $Co_{0.81}Ir_{0.19}$ film as an example, figure 3(a) shows a typical FMR spectrum (V'–H curve) with an RF signal (12 GHz, 20 dBm), where the external quasistatic magnetic field (H) is parallel to the RF current direction. Two resonance peaks with opposite polarity and an asymmetric line shape can be observed near $H = \pm 0.8$ kOe . The measured signal is fitted with the sum of the derivatives of the Lorentzian and anti-Lorentzian functions [33, 34]:

$$V' = -S\frac{\Delta H(H-H_0)}{\left[(H-H_0)^2+(\Delta H/2)^2\right]^2} + A\frac{(H-H_0)^2-(\Delta H/2)^2}{\left[(H-H_0)^2+(\Delta H/2)^2\right]^2} \quad (1)$$

where H_0 is the resonance position, while ΔH is the linewidth. S and A are the amplitudes for the Lorentzian and anti-Lorentzian terms, respectively. H_0 and ΔH can be obtained from the fitting; in the displayed curve, $H_0 = 0.748$ kOe and $\Delta H = 0.154$ kOe for the peak in positive field range. Here, we only consider H_0. The V'–H curves measured

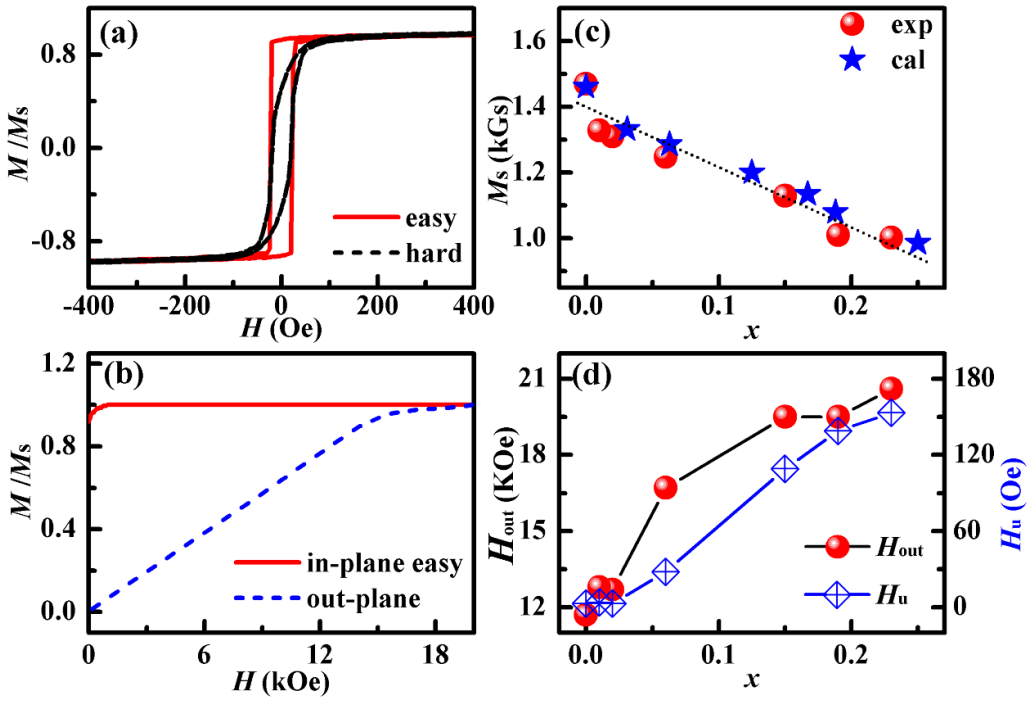

Figure 2. (a) Hysteresis loops along both easy axes (red line) and hard axes (black dashed line) in the film plane for the $Co_{0.94}Ir_{0.06}$ film. (b) Initial magnetization curves parallel (red line) and perpendicular (blue dashed line) to the film plane for the $Co_{0.94}Ir_{0.06}$ film. (c) The composition dependence of saturation magnetizations (M_s) for the $Co_{1-x}Ir_x$ films. The experimental values and calculation results are displayed using red round dots and blue five-pointed stars, respectively. The dotted line is for guidance. (d) The composition dependence of total out-of-plane anisotropy field H_{out} (red round dots) and in-plane uniaxial anisotropy field H_u (blue diamonds) for the $Co_{1-x}Ir_x$ films.

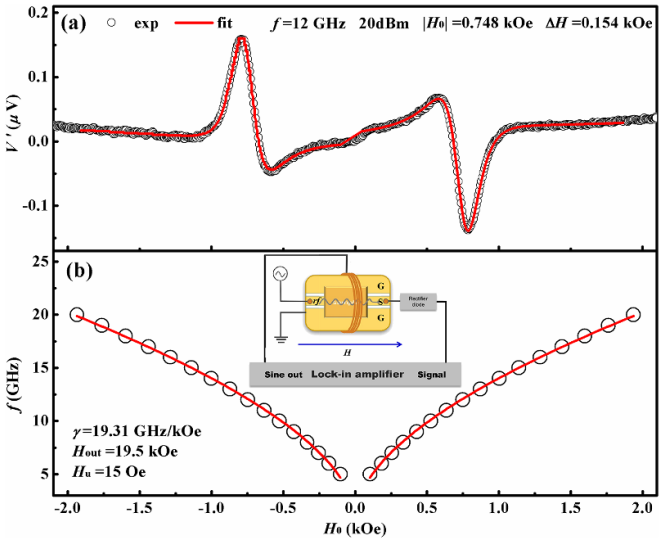

Figure 3. (a) Typical FMR resonance spectrum measured with external magnetic field H parallel to the RF current direction for the $Co_{0.81}Ir_{0.19}$ film. Open circles are raw data and curve indicates the line shape fitted using equation (1). (b) The relation between the frequency and the resonance position for the $Co_{0.81}Ir_{0.19}$ film. The open circles and the red curve represent the resonance positions of FMR obtained from the V'–H curves and the fitting line, respectively. The inset shows the schematic diagram of our FMR resonance system.

at different frequencies (5–20 GHz) were fitted, and the corresponding results of H_0 are denoted by open circles in figure 3(b). Obviously, H_0 shifts toward the high field range with increasing frequency. To determine the gyromagnetic ratio, we fitted H_0 using the Kittel equation [13]:

$$f = \frac{\gamma}{2\pi}\sqrt{(H_0 + H_u)(H_0 + H_u + H_{out})}. \quad (2)$$

The value of H_{out} mentioned above (in figure 2(d)) was used for the fitting. The value of H_u changes easily in the fitting, as the H_u in equation (2) is significantly affected by the angle between the in-plane easy axis and the long axis of the strip (the RF current direction). For example, in the fitting of the $Co_{0.81}Ir_{0.19}$ film in figure 3(b), the fitted value of H_u is much smaller than that in figure 2(d). However, when the RF current direction was parallel to the in-plane easy (hard) axis, the fitted value of H_u based on the new measured H_0 is 97 Oe (–115 Oe), which is closer to its value in figure 2(d). For consistency, we use the V'–H curves obtained with the RF current direction parallel to the long axis of the strips. As denoted by a red line in figure 3(b), the fitted curve coincides with the H_0 results obtained from the V'–H curves. From the fitting, we obtain the gyromagnetic ratio $\gamma = 19.31$ GHz kOe^{-1} for the $Co_{0.81}Ir_{0.19}$ film.

Similarly, γ is determined for the other $Co_{1-x}Ir_x$ films, and the results are displayed with red round dots in figure 4. The value of γ for the Co film is 19.13 GHz kOe^{-1}, smaller than the reported value for pure *hcp*-Co (19.16–19.28 GHz kOe^{-1}) [3, 32, 35]. This is owing to the anisotropy in γ [36], which is observed for all $Co_{1-x}Ir_x$ alloys in our calculation. Taking pure Co as an example, $\gamma = 19.15$ GHz kOe^{-1} along the x-axis, while $\gamma = 19.21$ GHz kOe^{-1} along the z-axis. As

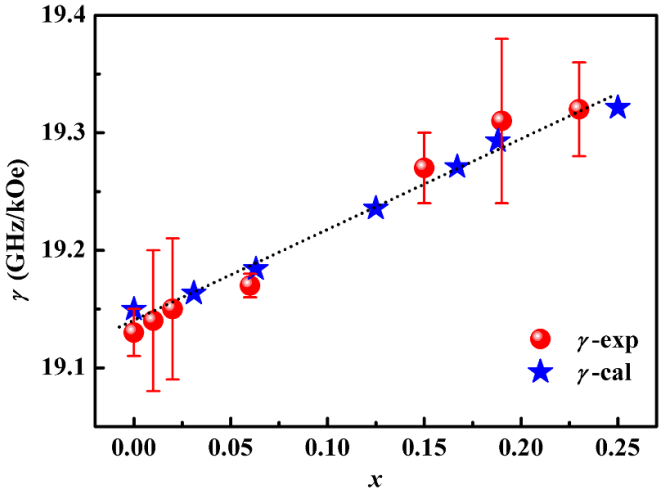

Figure 4. Composition dependence of the gyromagnetic ratio (γ) for the $Co_{1-x}Ir_x$ films. The experimental values and calculation results are represented by the red round dots and blue stars, respectively. The dotted line is for guidance.

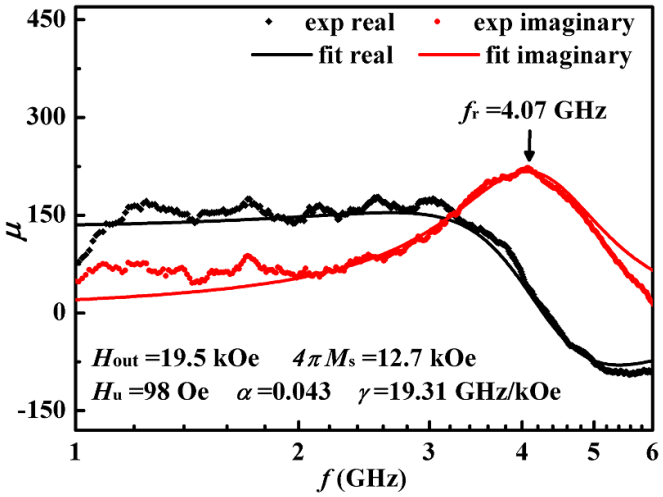

Figure 5. Complex permeability spectra of the $Co_{0.81}Ir_{0.19}$ film. The dots and the curves are experimental data and fitting results using equation (3), respectively.

the value of γ displayed in this study is in *ab*-plane, a smaller value is reasonable. γ in the CoIr films is larger than that in the Co film; it increases linearly from 19.14 GHz kOe^{-1} at $x = 0.01$–19.32 GHz kOe^{-1} at $x = 0.23$.

To verify the resulting γ, we measured the complex permeabilities of the $Co_{1-x}Ir_x$ films, and fitted them using the above results of γ and the same magnetic parameters in figure 2 (except for H_u, which changes in a suitable range). The fitting equations, obtained according to the Landau–Lifshitz–Gilbert equation, are as follows [9]:

$$\mu' = 1 + 4\pi M_s\gamma \frac{\omega_x^2\omega_y + \omega^2(\alpha^2\omega_y - \omega_x)}{[\omega_x\omega_y - (1+\alpha^2)\omega^2]^2 + \alpha^2\omega^2(\omega_x + \omega_y)^2} \quad (3a)$$

$$\mu'' = 4\pi M_s\gamma\alpha\omega \frac{\omega_x^2 + (1+\alpha^2)\omega^2}{[\omega_x\omega_y - (1+\alpha^2)\omega^2]^2 + \alpha^2\omega^2(\omega_x + \omega_y)^2} \quad (3b)$$

where $\omega_x = \gamma(H_{out} + H_u)$, $\omega_y = \gamma H_u$, $\omega = 2\pi f$, and α is the damping constant. Taking the $Co_{0.81}Ir_{0.19}$ film as an example, the measured complex permeability and the fitting results are shown in figure 5. Clearly, the fitting results agree well with the measurements, and the other films yield similar results. Consequently, the complex permeability fittings indicate that the value of γ obtained using equation (2) is reasonable.

3.2. Physical origin of the variation in γ

To understand the physical origin of the variation in γ, the magnetic and electronic properties of the *hcp* $Co_{1-x}Ir_x$ alloys are studied through first-principles calculation. The calculation results of lattice constant *c*, M_s, and γ along the *x*-axis are displayed using blue stars in the inset of figures 1, 2(c) and 4, respectively. Obviously, all the calculated results are consistent with the experimental results. Therefore, it is adequate

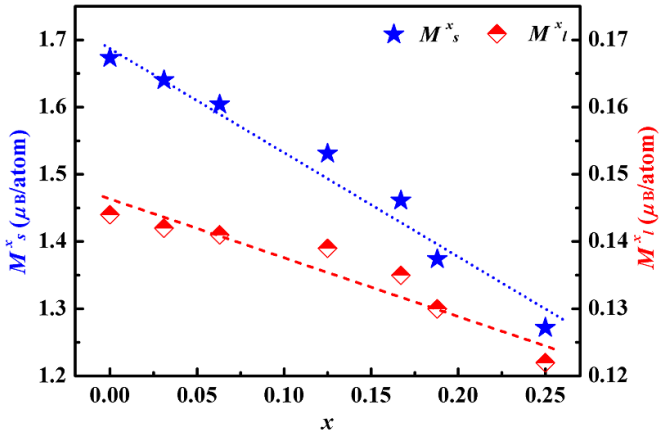

Figure 6. Composition dependence of total spin magnetic moments, M^x_s, (blue stars) and total orbital magnetic moments, M^x_l (red half-filled diamonds), with SO coupling parallel to the *x*-axis of the $Co_{1-x}Ir_x$ system. The dotted curves are for guidance. The changes in the M^x_l/M^x_s ratio indicate the increasing trend of γ on composition.

to deduce the physical mechanism of the variation trend in γ from the electronic structures of the system.

As is known, γ is proportional to the Landé *g* factor (*g*) via the relation $\gamma = g\frac{e\mu_0}{2m_e}$. Therefore, γ in the *ab*-plane is directly related to the ratio of the total orbital magnetic moment (M^x_l) and total spin magnetic moment (M^x_s) with SO coupling parallel to the *x*-axis of the system [21, 36], according to the Kittle equation $g = 2 + 2M^x_l/M^x_s$ [8, 35]. Thus, the values of M^x_s (M^x_l) was obtained by calculating the weighted average value of the local spin (orbital) moment for all atoms in the supercell of each CoIr case, and the results are displayed in figure 6. Generally, both the magnetic moments decrease linearly with increasing *x*, but M^x_s decreases faster, hence, resulting in the linear increase in γ.

For a more detailed explanation, we consider the local spin moment (m_s) and local orbital moment (m_l) of each atom, with the SO coupling parallel to the *x*-axis. The weighted average

Table 1. Weighted average value of spin magnetic moments (m_s, μ_B/atom) for Ir and its neighboring Co atoms, and those for the total number of Co atoms (tot-Co), in each x case with SO coupling parallel to the x-axis in the $Co_{1-x}Ir_x$ system.

x	tot-Co-m_s	Ir-m_s	Co1-m_s	Co2-m_s	Co3-m_s	Co4-m_s
0.00	1.673	—	1.673	—	—	—
0.03	1.679	0.433	1.567	1.635	1.700	1.707
0.06	1.680	0.468	1.586	1.677	1.732	1.724
0.13	1.679	0.459	1.641	1.669	1.822	—
0.17	1.667	0.452	1.639	1.753	—	—
0.19	1.577	0.496	1.538	1.633	1.754	—
0.25	1.538	0.473	1.538	1.539	—	—

Table 2. Weighted average value of orbital magnetic moments (m_l, μ_B/atom) for Ir and its neighboring Co atoms, and those for the total number of Co atoms (tot-Co), in each x case with SO coupling parallel to the x-axis in the $Co_{1-x}Ir_x$ system.

x	tot-Co-m_l	Ir-m_l	Co1-m_l	Co2-m_l	Co3-m_l	Co4-m_l
0.00	0.144	—	0.144	—	—	—
0.03	0.149	−0.070	0.162	0.149	0.147	0.143
0.06	0.160	−0.081	0.174	0.160	0.152	0.150
0.13	0.165	−0.046	0.169	0.164	0.162	—
0.17	0.175	−0.037	0.182	0.170	—	—
0.19	0.177	−0.074	0.181	0.179	0.146	—
0.25	0.187	−0.074	0.204	0.155	—	—

value of m_s for Ir and its neighboring Co atoms, and those for the total number of Co atoms (tot-Co), are listed in table 1, while the corresponding results of m_l are shown in table 2. Compared to the host Co atoms, Ir atoms have a significantly smaller value of m_s and m_l. This will induce linear decreasing trends of $M^x{}_s$ and $M^x{}_l$, owing to the increase in the relative number of Ir atoms with increasing x. However, as Ir has a negative value of m_l, a faster decrease in $M^x{}_l$ than that in $M^x{}_s$ should be observed, if only the variations in the local magnetic moment of Ir are taken into account, thereby inducing a reduction in γ with increasing x. This is diametrically opposed to the experimental result.

In view of this, we next focus on the local spin (orbital) magnetic moments of Co atoms. As shown in tables 1 and 2, the opposite trends in the weighted average value of m_s and m_l are observed for Co. Comparing with pure Co, a reduction in m_s is shown in Ir's neighboring Co atoms, and it gradually vanishes in those of the atoms farther from Ir. However, an increase in m_l for Ir's neighboring Co atoms is observed. For example, in $Co_{0.97}Ir_{0.03}$, the m_s are 1.567 μ_B/atom, 1.635 μ_B/atom and 1.700 μ_B/atom for the first (Co1), second (Co2), and third (Co3) nearest neighbors of Ir dopants, respectively; however, the m_l are 0.163 μ_B/atom, 0.149 μ_B/atom and 0.147 μ_B/atom for the Co1, Co2, and Co3 atoms, respectively. Alternatively, with increasing x, the values of m_s (such as for Co1) slightly decrease, while those of m_l significantly increase. The different trends in m_s and m_l for Ir's neighboring Co atoms induce the different observations of m_s and m_l for the total number of Co atoms (tot-Co), hence results in a faster decrease in $M^x{}_s$ than in $M^x{}_l$. Thus, the local magnetic moments of Ir's neighboring Co atoms are significant for the change of γ.

To understand the different behavior of m_s and m_l in Ir's neighboring Co atoms, we calculated the electronic densities of state (DOSs) of the Ir and Co atoms for each concentration, with the SO coupling parallel to the x-axis. Figure 7 shows the DOSs of Ir atoms and Ir's first nearest neighbor Co (Co1) atoms. For pure *hcp* Ir, no exchange splitting, and hence, no local spin moment, appears, which is different from the distinct splitting between the majority and minority spin states of pure *hcp* Co. When Ir is introduced to *hcp* Co, affected by the band structure of the host, exchange splitting appears in the Ir DOS, which results in a finite spin (orbital) moment for Ir. Moreover, the band structures of the host Co atoms are affected by the dopant. When Ir is introduced to *hcp* Co, lattice distortion centered at the Ir atoms appears, and it increases with increasing doping level [1]. For example, the bond lengths of Co2-Ir and Co1-Ir increase with x, whereas their ratio slightly decreases and then increases. The local lattice distortion alters the band structures of host Co atoms, particularly those of Ir's nearest neighbor Co atoms (Co1 and Co2 atoms), which are directly affected by the distortion, as the DOSs of Co1 atoms shown (black line in figure 7). The minority spin states of the Co1 DOSs move towards the low-energy side, and they are intensified with increasing x, which is significantly observed in the unoccupied minority spin states. This appearance reduces the exchange splitting between the majority and minority spin states, and hence leads to a reduction in the m_s of Co atoms. We observe that the appearance of the unoccupied minority spin states also plays an important role in the variation of m_l for Co atoms.

In the reported literature, which discuss the relation between the gyromagnetic ratio and spin (orbital) magnetic moment in the ferromagnetic/nonmagnetic (FM/NM) bilayer systems using band calculations, the changes in m_l are attributed to the d charge transfers from Cu (Pd) to Co (Ni) at the interface [21]. In view of this, we have calculated the occupation numbers of the d orbitals, and few charge transfers

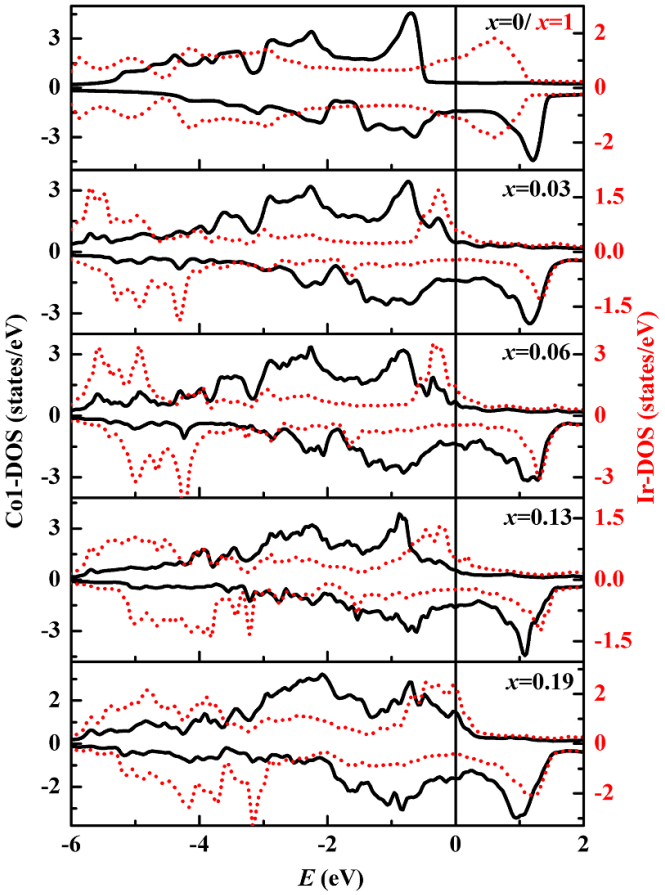

Figure 7. Total DOSs of Co1 (black line) and Ir (red dot line) atoms with SO coupling parallel to the x-axis in the $Co_{1-x}Ir_x$ system. The positive and negative directions represent the majority and minority spin states, respectively.

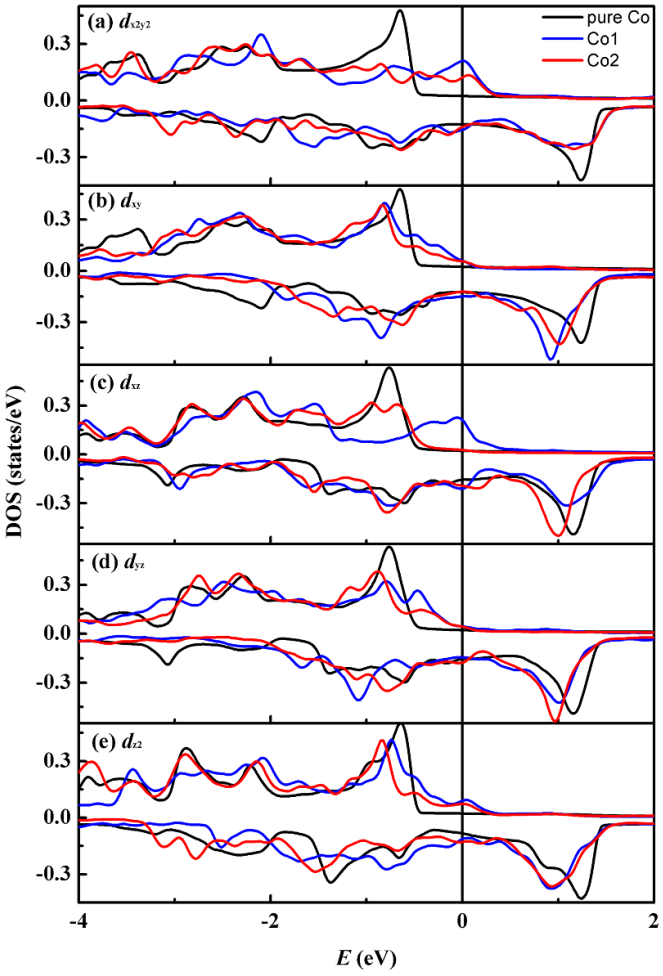

Figure 8. The d DOSs of Co1(blue line) and Co2 (red line) with SO coupling parallel to the x-axis for the $Co_{0.81}Ir_{0.19}$ alloy, as well as those of pure Co (black line).

occurred between atoms. Moreover, the number of electrons in each Co 3d suborbital is approximately equal. As the m_l of Co atoms primarily comes from 3d orbitals, the change in the m_l of Co atoms should arise from the evolutions of band structures of 3d suborbitals [1]. Hence, the DOSs of 3d suborbitals for Co atoms were calculated. As an example, figure 8 displays the 3d-DOSs of Co1 and Co2 atoms for the $Co_{0.81}Ir_{0.19}$ case, with the SO coupling parallel to the x-axis. Compared with those for pure Co, considerable variations in the appearance of 3d-DOSs for Co1 and Co2 can be clearly observed: both the occupied and unoccupied minority states of most 3d suborbitals move towards to the Fermi level, and particularly occurs for the unoccupied minority states.

In 3d transition metals and their alloys, the band widths of 3d orbitals (∼eV) are significantly larger than the energy scale of SO coupling (∼meV); therefore, the relativistic SO interaction can be regarded as a small perturbation to the electronic structure [37]. Hence, second-order perturbation theory is used to analyze the influence mechanism of SO coupling [37]. For example, the mechanisms of magnetocrystalline anisotropy energy are usually discussed through the perturbation expression of SO coupling induced energy [1, 38–40]. Inspired by this approach, we try to discuss the causes of the changes in m_l using the perturbation expression of orbital angular momentum. As discussed in [1], this system conforms to the conditions of second-order perturbation theory. Furthermore, as shown in figure 8, the majority spin states of Co are almost completely occupied, and the minority spin states are partially occupied. Therefore, the m_l of Co atoms along the x-axis (110-axis) can be approximated as [35]:

$$m_l = \mu_B \xi \sum_{o^-} \sum_{u^-} \frac{|\langle o^- | L_x | u^- \rangle|^2}{\delta \varepsilon_{u^- o^-}} \tag{4}$$

where $o^-(u^-)$ represents occupied (unoccupied) minority spin states, and $\delta\varepsilon_{u^-o^-} = \varepsilon_{u^-} - \varepsilon_{o^-}$ is the energy splitting between the corresponding occupied and unoccupied states. Lx is the x component of the orbital angular momentum operator. ξ and μ_B are the spin–orbit coupling constant and Bohr magneton, respectively. Although this formula is not sufficiently accurate to reproduce the value of m_l, it is adequate for interpreting the evolution.

In equation (4), the non-zero terms are $\left|\left\langle d_{z^2}{}^- | L_x | d_{yz}{}^- \right\rangle\right|^2$, $\left|\left\langle d_{x^2y^2}{}^- | L_x | d_{yz}{}^- \right\rangle\right|^2$ and $\left|\left\langle d_{xy}{}^- | L_x | d_{xz}{}^- \right\rangle\right|^2$. Neglecting the details of the band structures to conduct a qualitative discussion, the value of each term is determined by the energy

splitting $\delta\varepsilon_{u^-o^-}$. As mentioned above, due to the local lattice distortion centered at Ir, the unoccupied minority states of most 3*d* sub-orbitals move towards the Fermi level. Hence almost all the $\delta\varepsilon_{u^-o^-}$ values of non-zero terms for Ir's neighboring Co atoms decrease compared with those for pure Co atoms, particularly for Co1 and Co2 atoms. Consequently, according to equation (4), the m_l of Co atoms increase. As the left-shifts of the unoccupied minority states increase with increasing x, the reduction of $\delta\varepsilon_{u^-o^-}$, and in turn, the increase in m_l becomes more and more obvious.

4. Conclusion

C-axis oriented *hcp*-$Co_{1-x}Ir_x$ ($0.00 \leqslant x \leqslant 0.23$) films with good soft magnetic properties were successfully fabricated using magnetron sputtering. The experimental results of the structural and magnetic properties are in agreement with our theoretical results and previous literature. The γ of the *hcp* $Co_{1-x}Ir_x$ system was investigated according to the dc electric detection of FMR and first-principles calculations. γ increases linearly from 19.13 GHz kOe^{-1} at $x = 0.00$ to 19.32 GHz kOe^{-1} at $x = 0.23$ with increasing x. The results calculated using first-principles are in good agreement with the experimental results. The local magnetic moments calculations show that the variation in γ is due to the different behaviors in the spin and orbital magnetic moments of Ir's neighboring Co atoms: a slight decrease in m_s and a significant linear increase in m_l with increasing x. The electronic structure study indicates that the significant movements of the unoccupied minority spin states toward to the Fermi level, induced by the local lattice distortion centered at Ir, is crucial for the changes in m_s and m_l of Co atoms. As exhibited by the movements of the upoccupied minority spin states, the decreasing exchange splitting between majority and minority spin states induces a slight decrease in the m_s of Ir's near neighbor Co atoms. The movements also lead to a decrease in the energy splitting between corresponding occupied and unoccupied minority spin states, hence increasing the m_l of Co atoms. Our results supplement the important γ data for *hcp*-$Co_{1-x}Ir_x$ soft magnetic films, and will provide guidance in the understanding of the behaviors of γ and dynamic magnetic properties in disordered binary magnetic alloys.

Data availability statement

The data that support the findings of this study are available upon reasonable request from the authors.

Acknowledgments

This work is supported by the National Natural Science Foundation of Ningxia in China (2020AAC03238), the National Natural Science Foundations of China (Nos. 11574122, 51731001) and the Fundamental Research Funds for the Central Universities (No. lzujbky- 2017-k20). We would like to thank Editage for the English language editing.

ORCID iDs

Sha Zhang https://orcid.org/0000-0002-1215-3368
Zhiwei Li https://orcid.org/0000-0003-2239-2802

References

[1] Zhang S, Pang H, Hai L, Li W, Wang T and Li F 2019 First-principles study of the easy-plane magnetocrystalline anisotropy in bulk hcp $Co_{1-x}Ir_x$ *J. Appl. Phys.* **126** 083907
[2] Jiao J, Wang T, Ma T, Wang Y and Li F 2017 Achievement of diverse domain structures in soft magnetic thin film through adjusting intrinsic magnetocrystalline anisotropy *Nanoscale Res. Lett.* **12** 21
[3] Rinkevich A B, Samoilovich M I, Klescheva S M, Perov D V, Burkhanov A M and Kuznetsov E A 2014 Millimeter-wave properties and structure of gradient co-ir films deposited on opal matrix *IEEE Trans. Nanotechnol.* **13** 3–9
[4] Ma T, Jiao J, Li Z, Qiao L, Wang T and Li F 2017 Micrometer thick soft magnetic films with magnetic moments restricted strictly in plane by negative magnetocrystalline anisotropy *J. Magn. Magn. Mater.* **444** 119–24
[5] Xu F, Wang T, Ma T, Wang Y, Zhu S and Li F 2016 Enhanced film thickness for Néel Wall in soft magnetic film by introducing strong magnetocrystalline anisotropy *Sci. Rep.* **6** 20140
[6] Higuchi M, Hamal D B, Shrestha A and Higuchi K 2019 Reduced effective g-factor in graphene *J. Phys. Soc. Japan.* **88** 094707
[7] Hernandez F G G, Gusev G M and Bakarov A K 2013 Tuning of the landé g-factor in AlxGa1-xAs/ AlAs single and double quantum wells *J. Phys. Conf. Ser.* **456** 012015
[8] Schreiber F, Pflaum J, Frait Z, Mühge T and Pelzl J 1995 Gilbert damping and g-factor in Fe_xCo_{1-x} alloy films *Solid State Commun.* **93** 965–8
[9] Wang T, Zhang S, Xu F, Ma X, Zhang J and Li F 2016 The improvement of high-frequency magnetic properties in oriented hcp-$Co_{78}Ir_{22}$ soft magnetic films fabricated at high substrate temperature *J. Magn. Magn. Mater.* **406** 118–22
[10] Gharaati A and Khordad R 2012 Electron g-factor in quantum wire in the presence of Rashba effect and magnetic field *Superlattices Microst.* **51** 194–202
[11] Vaseghi B, Rezaei G and Malian M 2011 Energy levels and electron g-factor of spherical quantum dots with Rashba spin-orbit interaction *Phys. Lett.* A **375** 2747–53
[12] Fan X, Wang W, Wang Y, Zhou H, Rao J, Zhao X, Gao C, Gui Y S, Hu C M and Xue D 2014 Rapid characterizing of ferromagnetic materials using spin rectification *Appl. Phys. Lett.* **105** 262404
[13] Chen H, Fan X, Wang W, Zhou H, Gui Y S, Hu C M and Xue D 2013 Electric detection of the thickness dependent damping in $Co_{90}Zr_{10}$ thin films *Appl. Phys. Lett.* **102** 202410
[14] Shchepetilnikov A V, Nefyodov Y A, Kukushkin I V and Dietsche W 2013 Electron g-factor in GaAs/AlGaAs quantum wells of different width and barrier Al concentrations *J. Phys. Conf. Ser.* **456** 012035
[15] Li M, Feng Z B, Fan L, Zhao Y, Han H and Feng T 2016 The electron g factor in AlGaN/GaN quantum wells *J. Magn. Magn. Mater.* **403** 81–85
[16] Sandoval M A T *et al* 2018 Mesoscopic g-factor renormalization for electrons in III–V interacting nanolayers *Phys. Rev.* B **98** 075312
[17] Zamani A, Setareh F, Azargoshasb T and Niknam E 2017 Electronic structure and Landé g-factor of a quantum ring in the presence of spin-orbit coupling: temperature and Zeeman effect *Superlattices Microstruct.* **110** 243–51

[18] Kong W, Fan X, Zhou H, Cao J, Guo D, Gui Y S, Hu C M and Xue D 2016 Electrical detection of magnetization dynamics in an ultrathin CoFeB film with perpendicular anisotropy *Appl. Phys. Lett.* **109** 182406
[19] Zhou H, Fan X, Ma L, Zhang Q, Cui L, Zhou S, Gui Y S, Hu C M and Xue D 2016 Spatial symmetry of spin pumping and inverse spin hall effect in the Pt/ Y_3Fe_5 O_{12} system *Phys. Rev.* B **94** 134421
[20] Zhang Y, Fan X, Zhao X, Rao J, Zhou H, Guo D, Gui Y S, Hu C M and Xue D 2015 Angular dependent study on ferromagnetic resonance and spin excitations by spin rectification *J. Appl. Phys.* **117** 023905
[21] Lee J S, Vescovo E, Kao C C, Beaujour J M, Kent A D, Jang H, Kim J Y, Park J H and Shim J H 2009 Role of the nonmagnetic layer in determining the Landé g -factor in a spin-transfer system *Phys. Rev.* B **80** 180403
[22] Zhang S, Xu F, Ma X, Wang T, Tan G and Li F 2014 Thickness dependence of high-frequency magnetic properties in the oriented hcp-CoIr soft magnetic films with negative magnetocrystalline anisotropy *Appl. Surf. Sci.* **299** 81–85
[23] Wong H S, He S K, Chung H J, Zhang M S, Cher K, Low M, Zhou T J, Yang Y and Wong S K 2016 Reduction of magnetic damping and isotropic coercivity and increase of saturation magnetization in Rh-incorporated CoIr system *Nanotechnology* **27** 455705
[24] Hashimoto A, Saito S and Takahashi M 2006 A soft magnetic underlayer with negative uniaxial magnetocrystalline anisotropy for suppression of spike noise and wide adjacent track erasure in perpendicular recording media *J. Appl. Phys.* **99** 08Q907
[25] Nozawa N, Saito S, Kimura T, Shibuya K, Hoshino K, Hinata S and Takahashi M 2013 Atomic layer stacking structure and negative uniaxial magnetocrystalline anisotropy of $Co_{100-x}Ir_x$ sputtered films *J. Magn. Soc. Japan.* **37** 183–9
[26] Ma T Y, Jiao J Y, Li Z W, Qiao L, Wang T and Li F S 2018 Tuning the static and dynamic magnetic properties of c-axis oriented hcp-(CoIr) thin films by the addition of Cr *Appl. Surf. Sci.* **457** 598–603
[27] Xu F, Zhang S, Yang D, Wang T and Li F 2015 High-frequency properties of oriented hcp-$Co_{1-x}Ir_x$ ($0.06 \leqslant x \leqslant 0.24$) soft magnetic films *J. Appl. Phys.* **117** 17B725
[28] Hasegawa D, Nakasaka S, Sato M, Ogawa T and Takahashi M 2006 Magnetization process of h.c.p.-coir nanoparticles with negative uniaxial magnetocrystalline anisotropy *IEEE Trans. Magn.* **42** 2805–7
[29] Blaha P, Schwarz K, Madsen G, Kvasnicka D and Luitz J 2009 WIEN2k, an augmented plane wave plus local orbitals program for calculating crystal properties user's (available at: www.wien2k.at/reg_user/textbooks/usersguide.pdf) (Retrieved 19 October 2019)
[30] Perdew J P, Burke K and Ernzerhof M 1996 Generalized gradient approximation made simple(2) *Phys. Rev. Lett.* **77** 3865–8
[31] Takahashi M and Saito S 2008 Advanced granular-type perpendicular recording media *J. Magn. Magn. Mater.* **320** 2868–73
[32] Zhou H, Fan X, Wang F, Jiang C, Rao J, Zhao X, Gui Y S, Hu C M and Xue D 2014 Electric field controlled reversible magnetic anisotropy switching studied by spin rectification *Appl. Phys. Lett.* **104** 102401
[33] Xu J W and Kent A D 2020 Charge-to-spin conversion efficiency in ferromagnetic nanowires by spin torque ferromagnetic resonance: reconciling lineshape and linewidth analysis methods *Phys. Rev. Appl.* **14** 014012
[34] Lim Y, Khodadadi B, Li J F, Viehland D, Manchon A and Emori S 2021 Dephasing of transverse spin current in ferrimagnetic alloys *Phys. Rev.* B **103** 024443
[35] Stohr J and Siegmann H C 2010 *Magnetism from Fundamentals to Nanoscale Dynamics* (Berlin: Springer)
[36] Jhajhria D, Pandya D K and Chaudhary S 2016 Orbital moment probed spin orbit coupling effects on anisotropy and damping in CoFeB thin films *RSC Adv.* **6** 94717–22
[37] Steinbeck L, Richter M and Eschrig H 2001 Itinerant-electron magnetocrystalline anisotropy energy of YCo5 and related compounds *Phys. Rev.* B **63** 184431
[38] Wang D S, Wu R and Freeman A J 1993 First-principles theory of surface magnetocrystalline anisotropy and the diatomic-pair model *Phys. Rev.* B **47** 14932–47
[39] Dabrowski M *et al* 2014 Oscillations of the orbital magnetic moment due to d-band quantum well states *Phys. Rev. Lett.* **113** 067203
[40] Zhang W, Guo H T, Jiang J, Tao Q C, Song X J, Li H and Huang J 2016 Magnetism and magnetocrystalline anisotropy in single-layer $PtSe_2$: interplay between strain and vacancy *J. Appl. Phys.* **120** 013904